

1 **Revision 1**

2 **Bonding and electronic changes in rhodochrosite at high pressure**

3 **Gabriela A. Farfan,^{1*} Eglantine Boulard,¹ Shibing Wang,^{1,2} and Wendy L. Mao^{1,3}**

4 ¹Geological and Environmental Sciences, Stanford University, Stanford, California 94305,
5 U.S.A.

6 ²SSRL, SLAC National Accelerator Laboratory, Menlo Park, California 94025, U.S.A.

7 ³Photon Science, SLAC National Accelerator Laboratory, Menlo Park, California 94025, U.S.A.

8 * Present address: Department of Geological and Environmental Sciences, Stanford University,
9 Stanford, CA 94309, U.S.A. E-mail: gfarfan@stanford.edu

10 **Abstract**

11 Rhodochrosite (MnCO₃) exhibits a series of high pressure transitions between 15 GPa and 30
12 GPa and at 50 GPa at ambient temperature as observed by *in-situ* Raman spectroscopy, X-ray
13 diffraction (XRD), and X-ray emission spectroscopy (XES). A transition is observed to begin at
14 15 GPa and complete at 30 GPa which may be due to a number of possibilities: modifications in
15 the magnetic order, changes in the compression mechanism, and/or a structural transition
16 resulting from disorder. We also observed a first order phase transition of MnCO₃ at 50 GPa
17 which is not accompanied by any changes in the electronic spin state. These results highlight the
18 unique behavior of MnCO₃ which we found to be quite different from other common carbonates
19 such as siderite, magnesite and calcite.

20 **Keywords**

21 rhodochrosite, deep carbon, Raman spectroscopy, XES, XRD, high pressure, carbonate

22

23

24 **Introduction**

25 Understanding the behavior of carbon-rich phases in Earth's lower mantle is critical for
26 modeling the global carbon cycle, since the lower mantle is estimated to contain a hundred times
27 the carbon in our planet's outersphere (Hirschmann, 2006; Dasgupta and Hirschmann, 2010). In
28 the mantle, carbon is expected to be present as accessory phases (e.g. carbonate minerals,
29 graphite or diamond) due to its very low solubility in mantle silicate minerals (Keppler et al.,
30 2003; Shcheka et al., 2006). A number of high-pressure studies have investigated the stability of
31 carbonates for a large range of compositions: e.g. CaCO_3 (Dickens and Bowen, 1970; Ono et al.,
32 2005, 2007), MgCO_3 (Isshiki et al., 2004; Boulard et al., 2011), FeCO_3 (Lavina et al., 2009,
33 2010; Boulard et al., 2012). These studies demonstrate the importance of the nature of the cation
34 on the structures of high-pressure phases and their pressure-temperature stability field. Mn^{2+} has
35 a cation size between that of Mg^{2+} and Ca^{2+} , which could make rhodochrosite (MnCO_3) a
36 potential model compound for understanding the differences in the high pressure behaviors of
37 Mg and Ca carbonates. Mn is also a 3d transition metal which can have a variety of valence and
38 spin states like Fe in FeCO_3 .

39 To date, few studies have been conducted on MnCO_3 at high pressure. At ambient
40 conditions, MnCO_3 crystallizes in the $R\bar{3}c$ {note to typesetting, in all instances like this, the
41 minus sign is an overbar on top of the 3 (or other number)} structure typical of calcite group
42 carbonates. Santillán and Williams (2004) reported that this structure is stable up to at least 54
43 GPa using high pressure infrared (IR) spectroscopy and X-ray diffraction (XRD). More recently,
44 Ono et al. (2007) reported a phase transition at 50 GPa using XRD coupled with *in situ* laser
45 heating. Here we present results on the high pressure bonding and electronic behavior of MnCO_3

46 studied *in-situ* to over 50 GPa using Raman spectroscopy, XRD and X-ray emission
47 spectroscopy (XES).

48

49 **Experimental details**

50 Our starting material was a natural rhodochrosite sample from the Sweet Home Mine,
51 Alma, CO. From electron micro-probe analysis we determined the composition to be very pure,
52 $(\text{Mn}_{0.976}\text{Fe}_{0.012}\text{Mg}_{0.004}\text{Ca}_{0.002})\text{CO}_3$, with an uncertainty of approximately 1% in the cation
53 concentrations. In the rest of the text we will refer to this sample as MnCO_3 .

54

55 ***Raman Spectroscopy***

56 We collected *in situ* high pressure Raman spectra of MnCO_3 using a Renishaw RM1000
57 Raman microscope in the Extreme Environments Laboratory at Stanford University. This system
58 uses a 514 nm laser excitation line and has 4 cm^{-1} spectral resolution and $2\text{ }\mu\text{m}$ spatial resolution.
59 A small single crystal chip of MnCO_3 was loaded into a stainless steel gasket with a $120\text{ }\mu\text{m}$
60 diameter sample chamber into a symmetric diamond anvil cell (DAC) with 300 micron culets.
61 We used silicone oil as the pressure-transmitting medium, and the ruby fluorescence method was
62 used for determining the pressure (Mao et al., 1986). Raman spectra were collected up to 54 GPa
63 with a pressure step of about 2 GPa.

64

65 ***X-ray diffraction***

66 Synchrotron XRD spectra were collected *in situ* at the high pressure beamline 12.2.2 of
67 the Advanced Light Source (ALS), Lawrence Berkeley National Laboratory (LBNL). A
68 powdered sample of MnCO_3 was loaded into a symmetric DAC between two layers of NaCl and

69 in a Re gasket. NaCl was used as the pressure transmitting medium and its equation of state was
70 used to determine pressure. The sample was compressed at ambient temperature up to 47 GPa.
71 Angle dispersive XRD measurements were collected using a monochromatic incident X-ray
72 beam ($\lambda = 0.6199 \text{ \AA}$) at each step of pressure of ~ 5 GPa. The diffraction images were integrated
73 with the Fit2D software (Hammersley et al., 1996), and the XRD patterns were then treated with
74 the General Structure Analysis System (GSAS) software package (Larson and Von Dreele, 2004)
75 using the LeBail method to identify the different phases and refine lattice parameters.

76

77 *X-ray Emission Spectroscopy*

78 The XES experiments were carried out at the beamline 16-IDD of the Advanced Photon
79 Source (APS), Argonne National Laboratory (ANL). A powdered sample of MnCO_3 was loaded
80 into the DAC sample chamber within a Be gasket. The pressure was measured using the ruby
81 fluorescence method before and after each XES measurement and was found to be stable within
82 about 3 GPa. The XES signal was collected at 90 degrees from the incident X-ray beam through
83 the Be gasket. The $\text{K}\beta$ emission line of Mn was scanned from 6450 to 6510 eV with a 0.4 eV
84 step size. XES spectra were collected between 0 and 54.3 GPa with ~ 5 GPa steps.

85

86 **Results**

87 *Raman Spectroscopy*

88 The Raman spectra showed four main peaks at ~ 200 , 300, 700 and 1100 cm^{-1} , which
89 correspond to four different vibrational modes in the CO_3^{2-} group (Fig. 1). The modes with lower
90 wave numbers correspond to external modes associated with lattice vibrations that cannot be
91 described in terms of molecular units. In first approximation, these modes involve relative

92 motions of the molecular unit CO_3^{2-} in the surrounding lattice: a translational E_g mode at ~ 201
93 cm^{-1} (T) and a librational E_g mode at $\sim 302 \text{ cm}^{-1}$ (L). The higher frequency modes correspond to
94 internal modes which are restricted to vibrations within the CO_3^{2-} : an in-plane asymmetric
95 stretching E_g mode at $\sim 723 \text{ cm}^{-1}$ (ν_4) and a symmetric stretching A_{1g} mode at $\sim 1100 \text{ cm}^{-1}$ (ν_1).

96 All of the modes systematically increased in frequency with increasing pressure (Table
97 1). The $\delta \ln \nu / \delta P$ was significantly larger for the external E_g modes (Table 1, Fig. 2). In the
98 compression data, we observed an abrupt step in the Raman shift of the ν_1 mode at 15 GPa, and
99 again above 48 GPa where it develops a new higher frequency peak at the expense of the original
100 peak intensity (Figs. 3,4). These discontinuities were less obvious in the decompression data
101 (Fig. 4). The full width half maximum (FWHM) of the ν_1 mode increases from 0 to 15 GPa and
102 drops gradually until approximately 30 GPa, at which point it increases again until nearly 50 GPa
103 (Fig.5).

104

105 *X-Ray Diffraction*

106 At low pressure the diffraction pattern can be indexed by a combination of NaCl, Re
107 (from the gasket) and MnCO_3 , with $a = 4.78 \text{ \AA}$ and $c = 15.67 \text{ \AA}$ at 0.8 GPa which is in good
108 agreement with previous work (e.g. Graf, 1961). The XRD patterns taken under compression
109 indicate that the $R-3c$ structure is stable up to 15 GPa. The relative axial compressibilities of a/a_0 ,
110 c/c_0 and the axial ratio of c/a are shown in Figure 6. As observed in other carbonate series
111 minerals, the c axis is much more compressible than the a axis leading to a c/a ratio that decrease
112 with pressure (e.g. Lavina et al., 2010). Figure 7 shows the evolution of the d -spacing for the
113 three first diffraction peaks (012), (110) and (01-4) {note to typesetting: in all instances like this,
114 the minus sign is an overbar on top of the 4 (or other number)} with pressure. A change in the

115 slope is observed between 15 and 30 GPa, where the d -spacings of the (110) and (012)
116 diffraction peaks remain constant at 2.34 and 3.54 Å respectively, while other diffraction peaks
117 such as the (01-4), (113) or (02-2) continue to decrease in d -spacing with pressure. Due to this
118 peculiar evolution of the diffraction peak position, the XRD patterns of MnCO₃ above 15 GPa
119 cannot be fit to a rhombohedral structure. Above 30 GPa, the d -spacings of all of the diffraction
120 peaks decrease with pressure.

121

122 *X-Ray Emission Spectroscopy*

123 Figure 8 shows the evolution of the Mn Kβ XES spectra with increasing pressure between 0 and
124 54.3 GPa. The Kβ emission spectrum can be divided into a main line Kβ_{1,3} and a satellite line
125 Kβ' which appears at lower energy due to the exchange interaction between the 3*p* core hole and
126 the unfilled 3*d* shell in the final state of the emission process. The energy separation between the
127 satellite and the main line is proportional to the strength of the exchange interaction and the
128 intensity of the satellite peak is proportional to the net spin of the 3*d* shell (e.g. Badro et al.,
129 1999, 2003). Figure 8a shows XES spectra collected at 0 and 54.3 GPa. We did not observe a
130 collapse of this satellite peak intensity, which indicates that the high spin to low spin transition of
131 Mn²⁺ has not occurred up to at least 54 GPa. However, we did notice a reduction of the intensity
132 of the Kβ' shoulder, which is also reflected by the red shift of the Kβ_{1,3} main peak with pressure.
133 Figure 8b shows the evolution of the energy of the main peak Kβ_{1,3} under compression. The
134 energy of the peak Kβ_{1,3} decreases from 6490.4 to 6490.0 eV while going from 0 to 30 GPa,
135 above which no more changes were observed.

136

137

138 Discussion

139 *High pressure behavior of MnCO₃*

140 Our data suggest that MnCO₃ undergoes a series of changes at high pressure. MnCO₃ in the
141 *R-3c* structure is stable up to 15 GPa. The *a*-axis contracts by 2 % while the *c*-axis shrinks by
142 6.1% between 0.8 and 15.4 GPa. This difference of compressibility between the two axes is also
143 reflected in the Raman measurements. The relative changes in the Raman shift with increasing
144 pressure ($\delta \ln \nu / \delta P$) describe how sensitive a particular vibrational mode is to changes in pressure.
145 Two external modes are the most sensitive to changes of the unit cell in pressure: The L (E_g)
146 mode (Raman shift of approximately 300 cm⁻¹), an asymmetric vibration perpendicular to the
147 CO₃²⁻ plane and with the steepest $\delta \ln \nu / \delta P$ of 0.0131 GPa⁻¹, and the T (E_g) mode (Raman shift of
148 approximately 200 cm⁻¹), a symmetric vibrational mode which is also sensitive to changes in
149 pressure with a $\delta \ln \nu / \delta P$ of 0.0125 GPa⁻¹. These modes change the most with pressure because
150 they represent vibrations along the *c* axis, which are more sensitive to external pressure than the
151 other modes that are in the (*a,b*) plane. This is in contrast to the internal mode ν_1 (the most
152 prominent Raman mode in carbonates with a ~1100 cm⁻¹ Raman shift) which represents an
153 asymmetric stretching of the oxygens around the central carbon ion and the ν_4 mode (Raman
154 shift of ~700 cm⁻¹) which represents an asymmetric stretching of the CO₃²⁻ group with two of the
155 oxygens moving away from each other in the same plane as the CO₃²⁻. Both of these modes are
156 relatively insensitive to pressure with the $\delta \ln \nu / \delta P$ values of the ν_1 and ν_4 modes almost flat at
157 0.0017 and 0.0011 GPa⁻¹ respectively.

158 At 15 GPa we see evidence for the beginning of a transition with an abrupt ~10 cm⁻¹ step
159 increase in Raman shift of both ν_1 and ν_4 modes, indicating stiffening of the CO₃²⁻ bonds. The
160 FWHM of the ν_1 mode also reaches a maximum (~2.75 cm⁻¹) at this pressure. This transition was

161 also confirmed by the changes in the XRD patterns. Although no new XRD peaks were
162 observed, the XRD patterns can no longer be fitted by the rhombohedral structure. The d -spacing
163 of the (110) XRD peak is constant between 15 and 30 GPa, which indicates that the a axis does
164 not evolve. Structurally, the a parameter is related to the Mn^{2+} - Mn^{2+} distance and the c parameter
165 is related to the Mn^{2+} - CO_3^{2-} distance. Therefore, the volume change of the unit cell results from
166 shrinkage of the Mn^{2+} - CO_3^{2-} distance. From 15 to 30 GPa, the Raman spectra and XRD show a
167 linear evolution. The FWHM of the ν_1 Raman mode decreases up to 30 GPa where it reaches its
168 lowest value ($\sim 1.75 \text{ cm}^{-1}$). At ~ 30 GPa, a small change in slope is observed for the ν_1 mode. A
169 break in the evolution of XRD peak positions with pressure is also observed. Finally, this
170 transition is accompanied by changes in the XES spectra. A continuous evolution in the $\text{K}\beta_{1,3}$
171 position and $\text{K}\beta'$ intensity is observed from 0 to 30 GPa and ceases above 30 GPa.

172 From these observations, we propose that MnCO_3 undergoes a phase transition at 15 GPa
173 that completes at 30 GPa. The rearrangement of the MnO_6 octahedra may be associated with
174 electronic/magnetic changes although not with a high spin to low spin transition, which might be
175 similar to the magnetic transition observed in MnO at 30 GPa (Yoo et al, 2005). The XRD
176 patterns show that this new phase is different from the known high-pressure polymorphs of other
177 carbonates. However, because of the small number of diffraction peaks in the range of d -
178 spacings observed, we were not able to solve the structure of this new high-pressure phase.

179 Ono (2007) performed a synchrotron XRD study using a DAC coupled with laser heating and
180 observed that MnCO_3 is stable up to approximately 50 GPa, at which point it transforms into the
181 new orthorhombic structure and undergoes a $\sim 5\%$ volume reduction. We were able to observe a
182 similar phase transition at 50 GPa using Raman spectroscopy but at ambient temperatures. While
183 Santillán and Williams (2004) observed no changes in the MnCO_3 structure at high pressure

184 using IR- spectroscopy (IR), our Raman spectroscopy study used a smaller step size and was able
185 to detect the discontinuities and anomalies in the vibrational frequency of the carbonate group.

186 *Comparison of MnCO₃ to other carbonates*

187 At high pressure, MnCO₃ behaves differently from other common carbonates in the
188 lithosphere and mantle. FeCO₃ undergoes an isostructural high spin to low spin transition with an
189 associated ~10% volume collapse around 50 GPa, instead of the series of transitions seen in
190 MnCO₃ (Lavina et al., 2009; Farfan et al., 2012). At the spin transition, a new lower frequency
191 peak appears in the Raman spectra of the ν_1 mode, indicating a relaxation of the CO₃²⁻ in FeCO₃,
192 contrasting the behavior of the CO₃²⁻ group in MnCO₃. Thus, despite being neighbors in the
193 periodic table and both being 3d transition metals, the carbonates for Fe and Mn display very
194 different high-pressure behavior. Reasons for this difference in behavior of Fe²⁺ and Mn²⁺ may
195 include the difference in their ionic radii (Fe²⁺, has a radius of 0.78 and Mn²⁺ has a radius of
196 0.83) and the difference in their electronic configurations ([Ar]3d⁵ for Mn²⁺ in rhodochrosite and
197 [Ar]3d⁶ for Fe²⁺ in siderite). However, even for isoelectronic Mn²⁺ and Fe³⁺, both with [Ar]3d⁵
198 electronic configuration, their compounds behave differently under pressure. For example,
199 pressure-induced spin-transition occurs at ~50 GPa for Fe₂O₃ (Badro et al., 1999, 2002; Wang et
200 al., 2010;) as opposed to at ~105 GPa for MnO (Rueff et al., 2005; Yoo et al., 2005). From our
201 XES experiment, Mn²⁺ in MnCO₃ shows no evidence for a spin transition up to 54 GPa. It may
202 take higher pressures to induce a spin transition in MnCO₃. The five 3d valence electrons of
203 Mn²⁺ are able to spread larger in space than those of Fe³⁺ (Mn²⁺ has a larger radius than Fe³⁺ and
204 a lower oxidation state). This would lead to a smaller crystal field splitting energy for Mn²⁺ in
205 MnCO₃, which would favor a high spin configuration over a wider pressure range, similar to
206 what occurs in FeO at high pressure (Badro et al., 1999; Pasternak et al., 1997; Ono et al. 2007).

207
208 In MnCO_3 , the Mn^{2+} radius (0.83 Å) lies between Mg^{2+} (0.72 Å) and Ca^{2+} (1 Å) in
209 carbonates which makes it a potential candidate for understanding the difference in high-pressure
210 phase behavior between Mg and Ca carbonates which are the two most abundant carbonates on
211 the surface of the planet. Several studies have shown that MgCO_3 and CaCO_3 display different
212 high-pressure behavior. Magnesite is stable up to at least 112 GPa at room temperature (Fiquet et
213 al., 2002; Isshiki et al., 2004; Boulard et al., 2011). Several high-pressure and high-temperature
214 phases have been reported: a monoclinic phase at 82 GPa-2350K (Boulard et al., 2011), an
215 orthorhombic phase above 115 GPa-2200 K (Isshiki et al., 2004) and a pyroxene structure is also
216 predicted by theoretical calculation above 160 GPa (Oganov et al, 2008). In contrast, calcite
217 transforms into aragonite (orthorhombic) above 2 GPa at high temperature (Suito et al., 2001).
218 However, at room temperature, CaCO_3 undergoes a series of metastable phase transitions during
219 compression. Calcite transforms into calcite II at 1.5 GPa and calcite II into calcite III at 2.2 GPa
220 (Bridgman, 1939; Singh and Kennedy, 1974; Merrill and Bassett, 1975). The structure of calcite
221 II differs slightly from calcite I by rotation of the CO_3^{2-} planar groups and a small displacement
222 of the Ca^{2+} cations from the adjacent CO_3^{2-} layer (Merrill and Bassett, 1975; Kawano et al.,
223 2009). The calcite II Raman spectrum is very similar to that of calcite with only a few new low
224 intensity peaks. The XRD patterns are also very similar. The structure of calcite III is still under
225 debate, with several structures having been proposed from different studies (Davis, 1964; Merrill
226 and Bassett, 1975; Smyth and Ahrens, 1997; Merlini et al., 2012).

227 A recent study on the solid solution between Mn and Ca carbonate observed
228 transformation of $(\text{Mn,Ca})\text{CO}_3$ into calcite II and calcite III structures for MnCO_3 contents up to
229 40% (Shi et al., 2012). They show a progressive increase in the pressure of the two phase

230 transitions with increasing MnCO_3 content. By extrapolating to 100% of MnCO_3 one would
231 expect rhodochrosite to transform into calcite II structure above 19 GPa and into calcite III above
232 26 GPa. In the present study we observed a phase transition at 15 GPa with a structure close to
233 rhodochrosite, which bears some similarities to the calcite-calcite II relationship. However, here
234 we did not observe any new XRD peaks and Raman peaks in MnCO_3 at 15 GPa. This could be a
235 result of the expected new peaks being too weak to be observed, or the high-pressure phase
236 structure reported here being different from the calcite II structure.

237 These features could also be interpreted as a change in the compression mechanism.
238 Similar to our observations of the a and c axes shrinkage, Fiquet et al. (1994) reported a change
239 in the slope of the axial compressibilities in MgCO_3 at 8 GPa at which point the c axis became
240 more compressible and the a axis less compressible while still maintaining the rhombohedral
241 structure. In this study we also observed that the a axis becomes incompressible as reflected by
242 the position of the XRD (110) reflection being fixed at 2.34 Å. However, in our experiment on
243 MnCO_3 , the change in axial compressibilities is associated with the loss of R-3c symmetry.

244 In summary, our *in-situ* Raman spectroscopy, XRD, and XES study reveals the intriguing
245 high pressure behavior of MnCO_3 , and highlights the contrasting behavior between the different
246 carbonate compositions as well as the need for further study to elucidate their complicated high
247 pressure electronic and bonding behavior.

248

249

250

251

252

253 **Acknowledgments**

254 We thanks Jinyuan Yan, Jason Knight and Alastair MacDowell for their assistance with XRD
255 experiments at ALS and Yuming Xiao and Paul Chow for their assistance with XES experiments
256 at APS. We also thank R. Jones for his assistance with the electron microprobe measurements,
257 M. Scott for providing the rhodochrosite samples, François Guyot for his helpful conversations,
258 Richard Nevle who organized the Stanford School of Earth Sciences Undergraduate Research
259 Program, and Associate Editor J. Kung and the anonymous reviewers. W.L. Mao and S. Wang
260 are supported by NSF, Geophysics Grants EAR-1141929. ALS is supported by the Office of
261 Science, Office of Basic Energy Sciences, and Materials Sciences Division of the U.S.
262 Department of Energy under contract DE-AC02-05CH11231. Portions of this work were also
263 performed at HPCAT (Sector 16), which is supported by DOE-NNSA, DOE-BES, and NSF.
264 APS is supported by DOE-BES, under Contract No. DE-AC02-06CH11357. X-ray diffraction
265 was performed at the high-pressure beamline 12.2.2 at the Advanced Light Source which is
266 supported by the Director, Office of Science, Office of Basic Energy Sciences, of the U.S.
267 Department of Energy under Contract No. DE-AC02-05CH11231. This research was partially
268 supported by COMPRES, the Consortium for Materials Properties Research in Earth Sciences
269 under NSF Cooperative Agreement EAR 11-57758. Eglantine Boulard acknowledges support
270 from the Deep Carbon Observatory.

271 **References cited**

- 272 Badro, J., V. V Struzhkin, J. Shu, R. J. Hemley, and H. Mao (1999) Magnetism in FeO at
273 Megabar Pressures from X-Ray Emission Spectroscopy, *Physical Review Letters*, 83(20),
274 4101–4104.
- 275 Badro, J., G. Fiquet, V. Struzhkin, M. Somayazulu, H. Mao, G. Shen, and T. Le Bihan (2002)
276 Nature of the High-Pressure Transition in Fe₂O₃ Hematite, *Physical Review Letters*, 89(20),
277 11–14.
- 278 Badro, J., G. Fiquet, F. Guyot, J.-P. Rueff, V. V Struzhkin, G. Vankó, and G. Monaco (2003)
279 Iron partitioning in Earth's mantle: toward a deep lower mantle discontinuity., *Science*
280 (New York, N.Y.), 300(5620), 789–91. Boulard, E., A. Gloter, A. Corgne, D. Antonangeli,
281 and A. Auzende (2011), New host for carbon in the deep Earth, *PNAS*, 108(13), 5184–
282 5187.
- 283 Boulard, E., Menguy, N., Auzende, A. L., Benzerara, K., Bureau, H., Antonangeli, D., Corgne,
284 A., Morard, G., Siebert, J., Perrillat, J. P., Guyot, F., Fiquet, G. (2012) Experimental
285 investigation of the stability of Fe-rich carbonates in the lower mantle, *Journal of*
286 *Geophysical Research*, 117(B2), 1–15
- 287 Bridgman, P. W. (1939) The high pressure behavior of miscellaneous minerals, *American*
288 *Journal of Science*, 237(1), 7–18.
- 289 Couture, L. (1947) Etude de spectres de vibrations de monocristaux ioniques, *Annales de*
290 *Physique*, 17, 88–122.

- 291 Dasgupta, R., and M. M. Hirschmann (2010) The deep carbon cycle and melting in Earth's
292 interior, *Earth and Planetary Science Letters*, 298(1-2), 1–13. Davis, B. L. (1964), X-ray
293 Diffraction Data on two high-pressure phases of calcium carbonate, *Science*, 145, 489–491.
- 294 Dickens, B., and S. Bowen (1970) Refinement of the crystal structure of the aragonite phase of
295 CaCO₃, *Journal of Research of the National Bureau of Standards A. Physics and Chemistry*,
296 75A, 27–32.
- 297 Farfan, G., S. Wang, H. Ma, R. Caracas, and W. L. Mao (2012) Bonding and structural changes
298 in siderite at high pressure, *American Mineralogist*, 97, 1421-1426.
- 299 Fiquet, G., F. Guyot, and J. Itié (1994) High-pressure X-ray diffraction study of carbonates□:
300 MgCO₃, CaMg(CO₃)₂ and CaCO₃, *American Mineralogist*, 79, 15–23.
- 301 Fiquet, G., F. Guyot, M. Kunz, J. Matas, D. Andrault, and M. Hanfland (2002) Structural
302 refinements of magnesite at very high pressure, *American Mineralogist*, 87, 1261–1265.
- 303 Graf, D. L. (1961) Crystallographic tables for the rhombohedral carbonates, *The American*
304 *Mineralogist*, 46, 1283–1316.
- 305 Hammersley, a. P., S. O. Svensson, M. Hanfland, a. N. Fitch, and D. Hausermann (1996) Two-
306 dimensional detector software: From real detector to idealised image or two-theta scan,
307 *High Pressure Research*, 14(4-6), 235–248.
- 308 Hirschmann, M. M. (2006) Water, Melting, and the Deep Earth H₂O Cycle, *Annual Review of*
309 *Earth and Planetary Sciences*, 34(1), 629–653. Isshiki, M., T. Irifune, K. Hirose, S. Ono, Y.

- 310 Ohishi, T. Watanuld, E. Nishibori, M. Takata, and M. Sakata (2004), Stability of magnesite
311 and its high-pressure form in the lowermost mantle, *Nature*, 427(January), 60–63.
- 312 Kawano, J., A. Miyake, N. Shimobayashi, and M. Kitamura (2009) Molecular dynamics
313 simulation of the phase transition between calcite and CaCO₃-II., *Journal of physics.*
314 *Condensed matter*: an Institute of Physics journal, 21(27), 275403.
- 315 Keppler, H., M. Wiedenbeck, and S. S. Shcheka (2003) Carbon solubility in olivine and the
316 mode of carbon storage in the Earth's mantle, 424, 414–416.
- 317 Larson, A. C., and R. B. Von Dreele (2004) General Structure Analysis System (GSAS), Los
318 Alamos National Laboratory Report LAUR, 86–748.
- 319 Lavina, B., P. Dera, R. T. Downs, V. Prakapenka, M. Rivers, S. Sutton, and M. Nicol (2009)
320 Siderite at lower mantle conditions and the effects of the pressure-induced spin-pairing
321 transition, *Geophysical Research Letters*, 36(23), L23306.
- 322 Lavina, B., P. Dera, R. Downs, W. Yang, S. Sinogeikin, Y. Meng, G. Shen, and D. Schiferl
323 (2010), Structure of siderite FeCO₃ to 56 GPa and hysteresis of its spin-pairing
324 transition, *Physical Review B*, 82(6), 064110.
- 325 Mao, H. K., J. Xu, and P. M. Bell (1986) Calibration of the Ruby Pressure Gauge to 800 kbar
326 under quasi-hydrostatic Conditions, *Journal of Geophysical Research*, 91(B5), 4673–4676.
- 327 Merlini, M., M. Hanfland, and W. a. Crichton (2012) CaCO₃-III and CaCO₃-VI, high-pressure
328 polymorphs of calcite: Possible host structures for carbon in the Earth's mantle, *Earth and*
329 *Planetary Science Letters*, 333-334, 265–271.

- 330 Merrill, B. L., and W. A. Bassett (1975) The Crystal Structure of CaCO_3 (II), a High-Pressure
331 Metastable Phase of Calcium Carbonate, *Acta Crystallographica*, B31, 343–349.
- 332 Oganov, A.R., Ono, S., Ma, Y., Glass, C.W., and Garcia, A. (2008) Novel high-pressure
333 structures of MgCO_3 , CaCO_3 and CO_2 and their role in earth's lower mantle. *Earth and*
334 *Planetary Science Letters*, 273, 38–47.
- 335 Ono, S. (2007) High-pressure phase transformation in MnCO_3 : a synchrotron XRD study,
336 *Mineralogical Magazine*, 71(1), 105–111.
- 337 Ono, S., T. Kikegawa, Y. Ohishi, and J. Tsuchiya (2005) Post-aragonite phase transformation in
338 CaCO_3 at 40 GPa, *American Mineralogist*, 90(4), 667–671.
- 339 Ono, S., T. Kikegawa, and Y. Ohishi (2007) High-pressure transition of CaCO_3 , *American*
340 *Mineralogist*, 92(7), 1246–1249.
- 341 Ono, S., Y., Ohishi, and T., Kikegawa (2007) High-pressure study of rhombohedral iron oxide,
342 FeO , at pressures between 41 and 142 GPa, *Journal of Physics Condensed Matter*, 19(3).
343 DOI:10.1088/0953-8984/19/3/036205.
- 344 Pasternak, P., Taylor, R., D., Jeanloz, R., Li, X., Nguyen, J. H. and McCammon, C. A. (1997)
345 High Pressure Collapse of Magnetism in $\text{Fe}_{0.94}\text{O}$: Mössbauer Spectroscopy Beyond 100
346 GPa, *Physical Review Letters*, 79, 5046–5049.
- 347 Rueff, J.P., a Mattila, J. Badro, G. Vankó, and a Shukla (2005) Electronic properties of
348 transition-metal oxides under high pressure revealed by x-ray emission spectroscopy,
349 *Journal of Physics: Condensed Matter*, 17(11), S717–S726.

- 350 Santillán, J., and Q. Williams (2004) A high-pressure infrared and X-ray study of FeCO₃ and
351 MnCO₃: comparison with CaMg(CO₃)₂-dolomite, *Physics of the Earth and Planetary*
352 *Interiors*, 143-144, 291–304.
- 353 Shcheka, S. S., M. Wiedenbeck, D. J. Frost, and H. Keppler (2006) Carbon solubility in mantle
354 minerals, , 245, 730–742.
- 355 Shi, W., M. E. Fleet, and S. Shieh (2012) High-pressure phase transitions in Ca-Mn carbonates
356 (Ca,Mn)CO₃ studied by Raman spectroscopy, *American Mineralogist*, 97, 999–1001.
- 357 Singh, A. K., and G. C. Kennedy (1974) Compression of Calcite to 40 kbar, *Journal of*
358 *Geophysical Research*, 79(17), 2615–2622.
- 359 Smyth, J. R., and T. J. Ahrens (1997) The crystal structure of calcite III, *Geophysical Research*
360 *Letters*, 24(13), 1595.
- 361 Suito, K., J. Namba, T. Horikawa, Y. Taniguchi, N. Sakurai, M. Kobayashi, A. Onodera, O.
362 Shimomura, T. Kikegawa, and T. A. K. Ikegawa (2001) Phase relations of CaCO₃ at high
363 pressure and high temperature, *American Mineralogist*, 86, 997–1002.
- 364 Wang, S. et al. (2010) High-pressure evolution of Fe₂O₃ electronic structure revealed by x-ray
365 absorption, *Physical Review B*, 82, 144428.
- 366 White, W. B. (1974) The carbonate minerals, in *The Infrared Spectra of Minerals: Mineralogical*
367 *Society of London Monograph 4*, edited by V. C. Farmer, pp. 227–284.

368 Yoo, C. et al. (2005) First-Order Isostructural Mott Transition in Highly Compressed MnO,
369 Physical Review Letters, 94(11), 115502.

370

371 **Figure captions:**

372

373 Figure 1: Raman spectra of MnCO₃ at ambient conditions. The main peaks include two external
374 E_g peaks: a T mode at approximately 201 cm⁻¹ and an L mode at approximately 300 cm⁻¹ as well
375 as two internal stretching modes: asymmetric stretching ν₄ mode at 700 cm⁻¹ and the symmetric
376 stretching ν₁ mode at approximately 1100 cm⁻¹.

377

378 Figure 2: Peak positions for the main E_g modes (T, L and ν₄) modes with increasing pressure.
379 The two vertical dashed lines indicate the range over which the 15-30 GPa transition was
380 observed.

381

382 Figure 3: Raman spectra of the ν₁ mode with increasing pressure. A new higher-frequency peak
383 starts to emerge at 48.2 GPa. The intensity of this new peak increases with increasing pressure at
384 the expense of the original peak.

385

386 Figure 4: Peak positions of the ν₁ mode with increasing pressure. The increasing pressure data
387 cycle is shown as filled circles and the releasing pressure cycle is shown as open circles. The
388 data uncertainties fall within the size of the markers. The dashed line at ~15 GPa outlines a break
389 in the slope in the increasing pressure data, which represents the beginning of a first phase
390 transformation which is completed at ~30 GPa (second dashed line). The peak splitting occurs at
391 around 48 GPa (outlined in a dashed line).

392

393 .

394

395 Figure 5: FWHM of the ν_1 , ν_4 , and T modes with increasing pressure to 50 GPa.

396

397 Figure 6: The relative axial compressibilities of a/a_0 (black squares), c/c_0 (open squares) and the
398 axial ratio of c/a (black dots) for the rhombohedral phase of MnCO_3 as a function of pressure.

399 Error on the lattice parameter from GSAS refinements fall within the symbols size.

400

401 Figure 7: XRD patterns collected at room temperature. Left: XRD pattern at 0.1 GPa, (hkl) of the
402 rhodochrosite peaks are indexed. Right: evolution of the d -spacing of these diffraction peaks.

403

404 Figure 8: a) XES collected at 0 (open squares) and 54.3 GPa (black circles). The intensities are
405 normalized so the maximum intensity of the main peak is 1. b) Energy of the main peak $K\beta_{1,3}$
406 with the pressure.

407

408

409

410

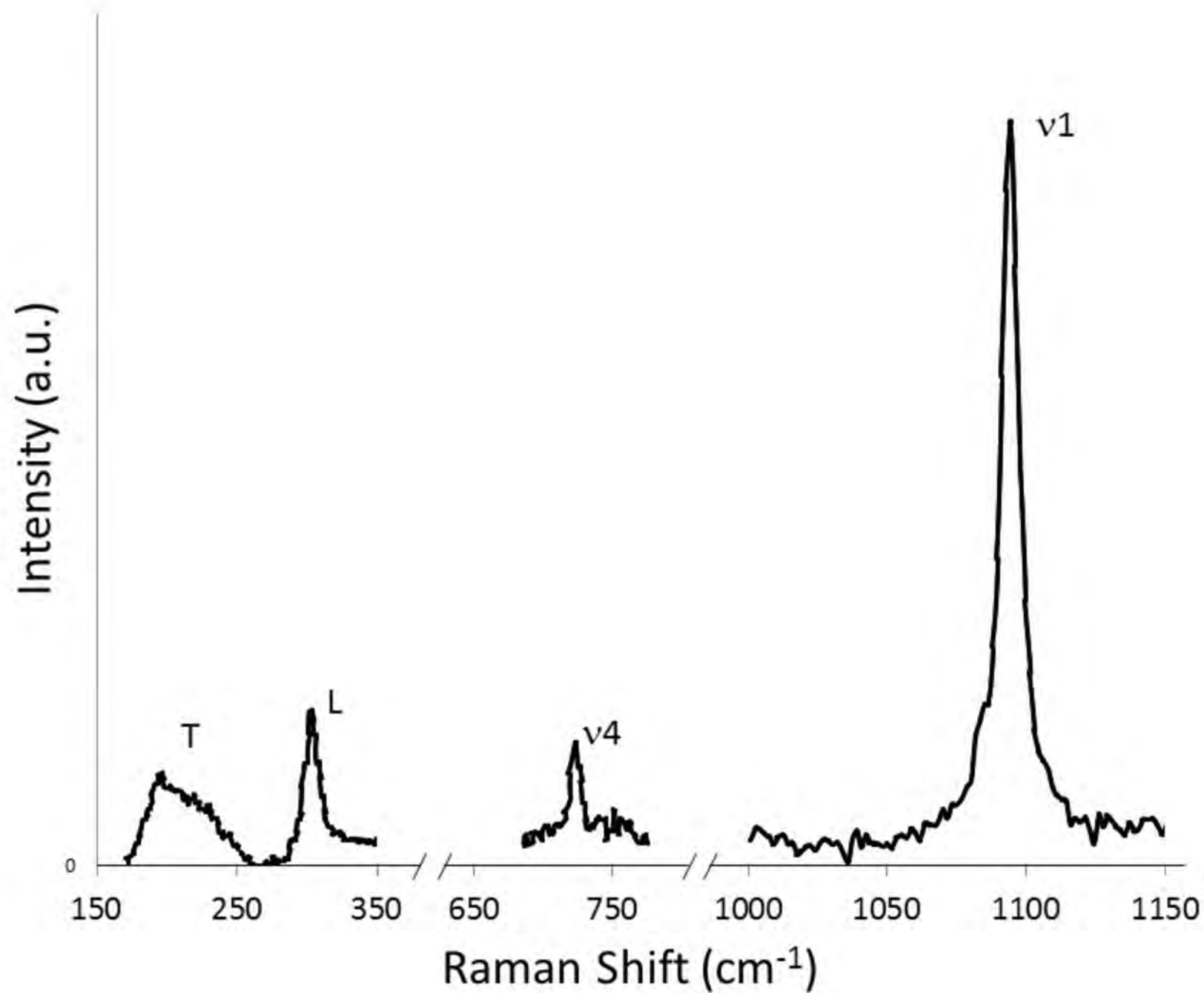
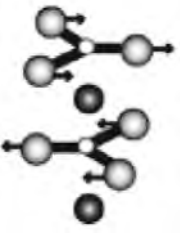
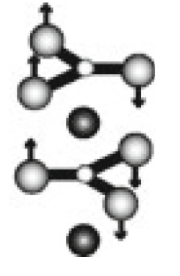
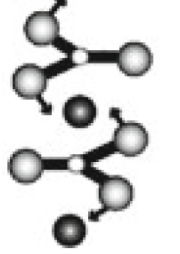




Figure 1

Table 1: Pressure dependence of Raman modes in MnCO₃.

Raman mode*	Frequency at ambient conditions (cm ⁻¹)	$\delta\nu/\delta P$ (cm ⁻¹ /GPa)	$\delta\ln\nu/\delta P$ (GPa ⁻¹)	Schematic of Raman modes (Boulard et al., 2012)
E _g (T) external symmetric vibration	201	2.685	0.0125	
E _g (L) external asymmetric vibration	302	4.147	0.0131	
E _g (ν ₄) internal asymmetric C-O stretching	723	0.946	0.0011	
A _{1g} (ν ₁) internal symmetric C-O stretching	1100	1.906	0.0017	
ν ₁ split	split peak at 48 GPa	2.339	0.0022	

* Raman group assignments from Couture (1947) and White (1974).

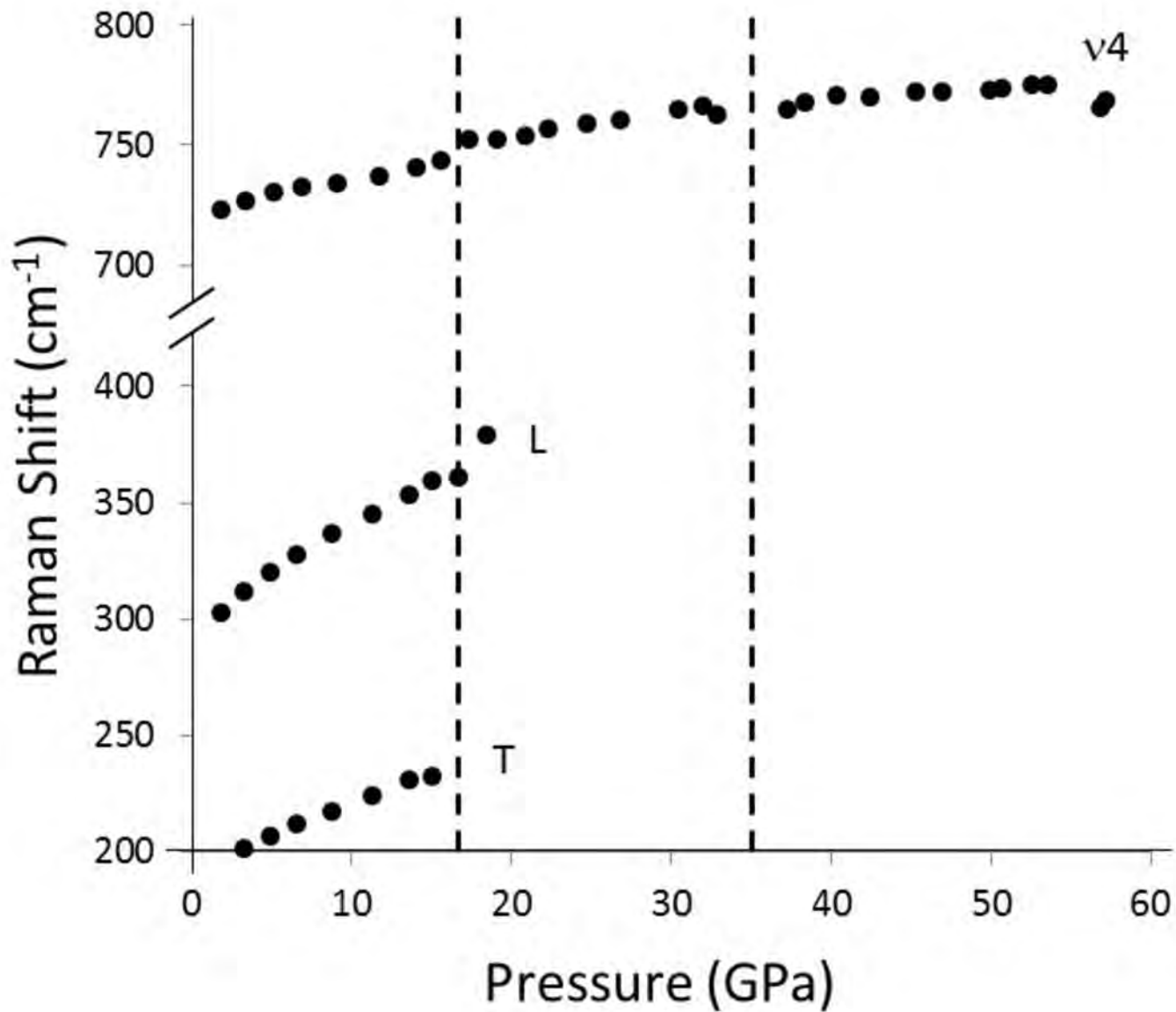


Figure 2

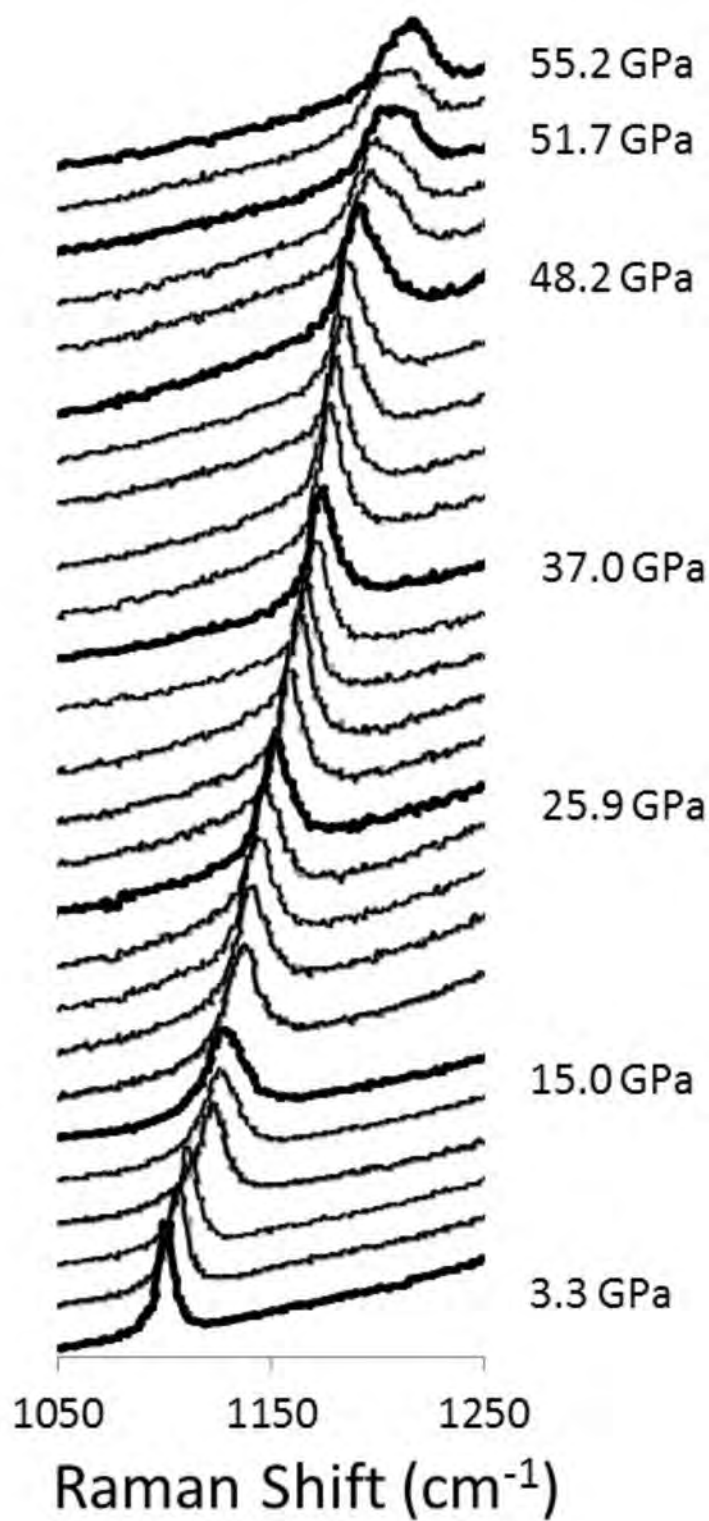


Figure 3

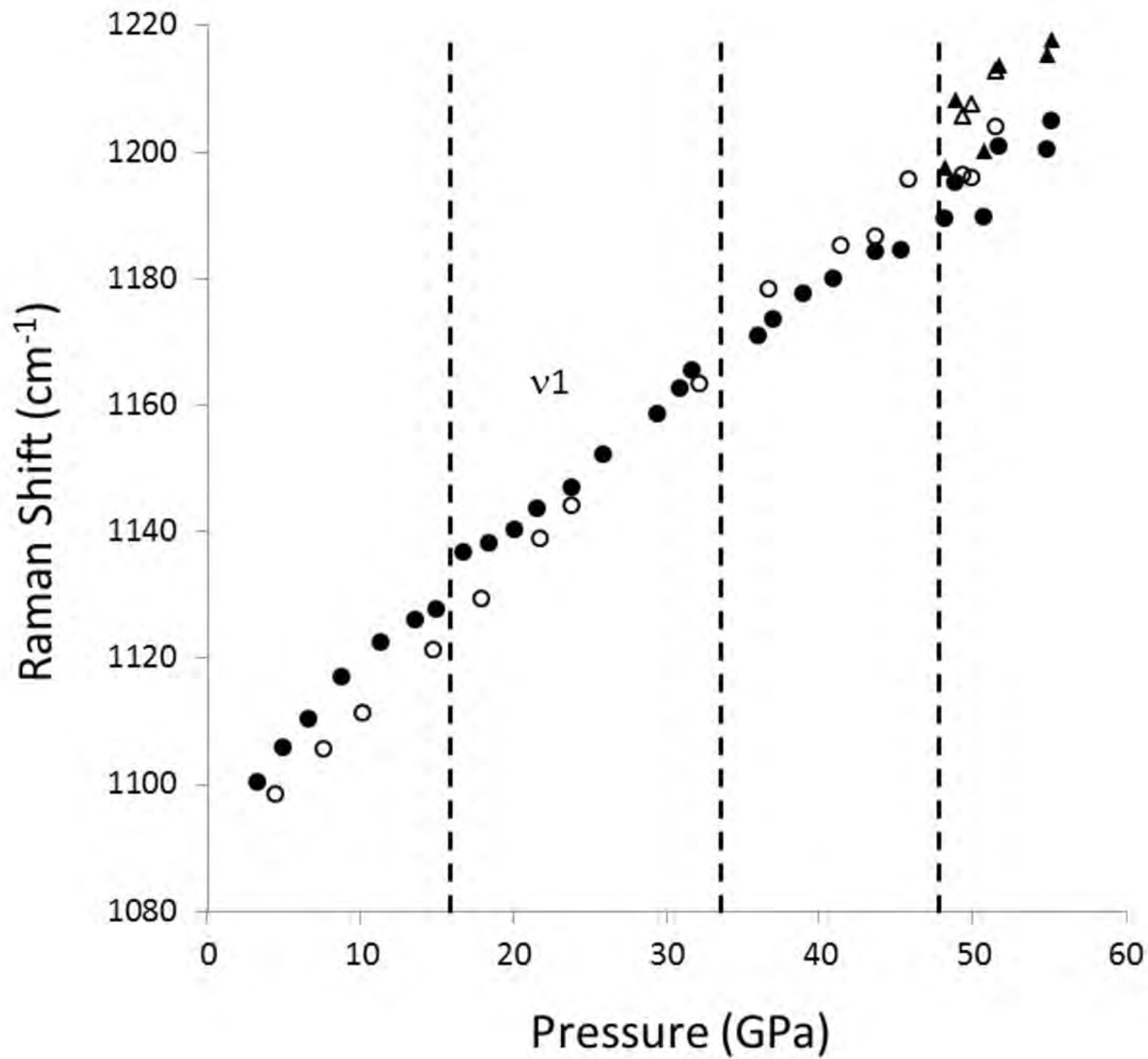


Figure 4

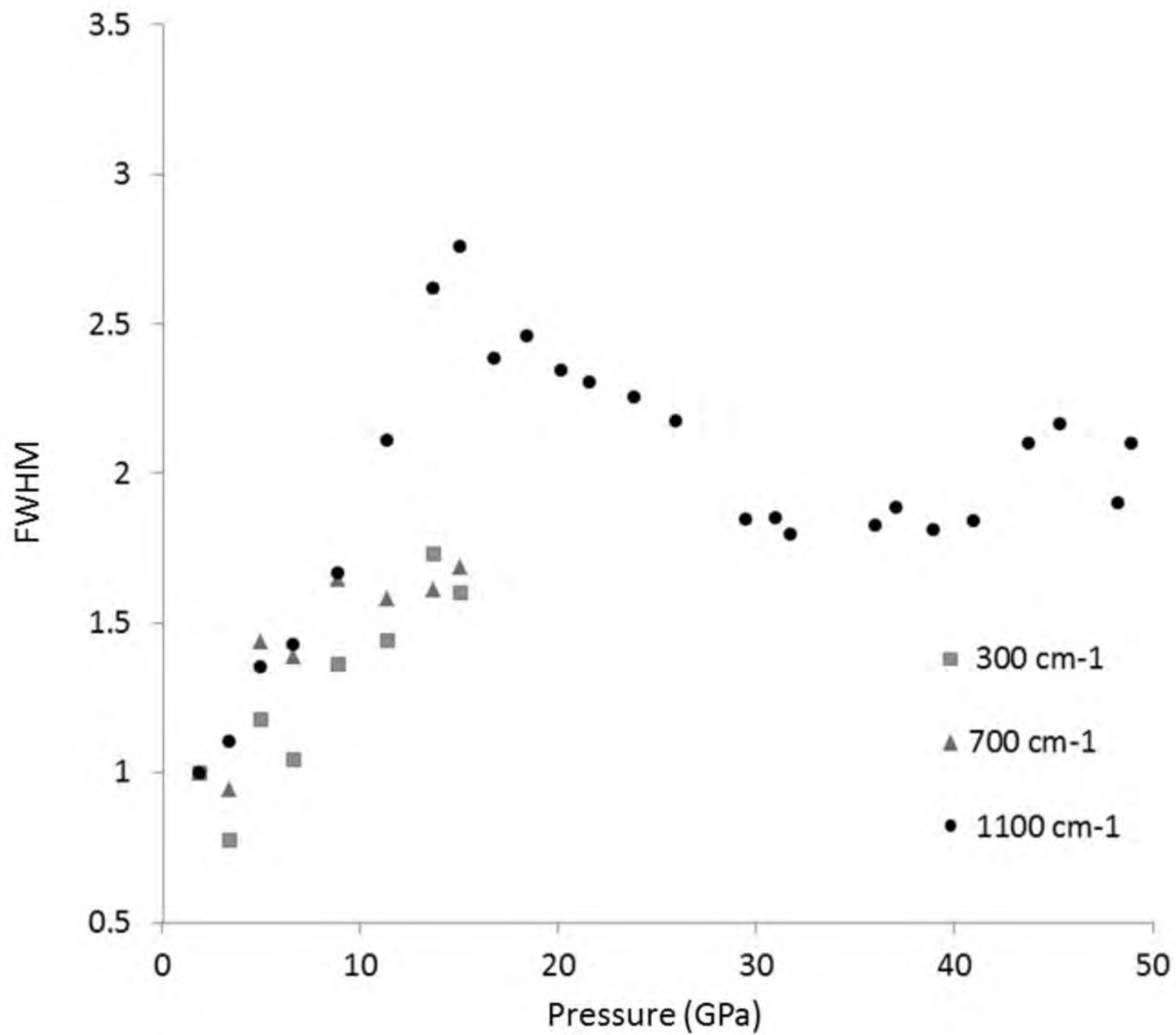


Figure 5

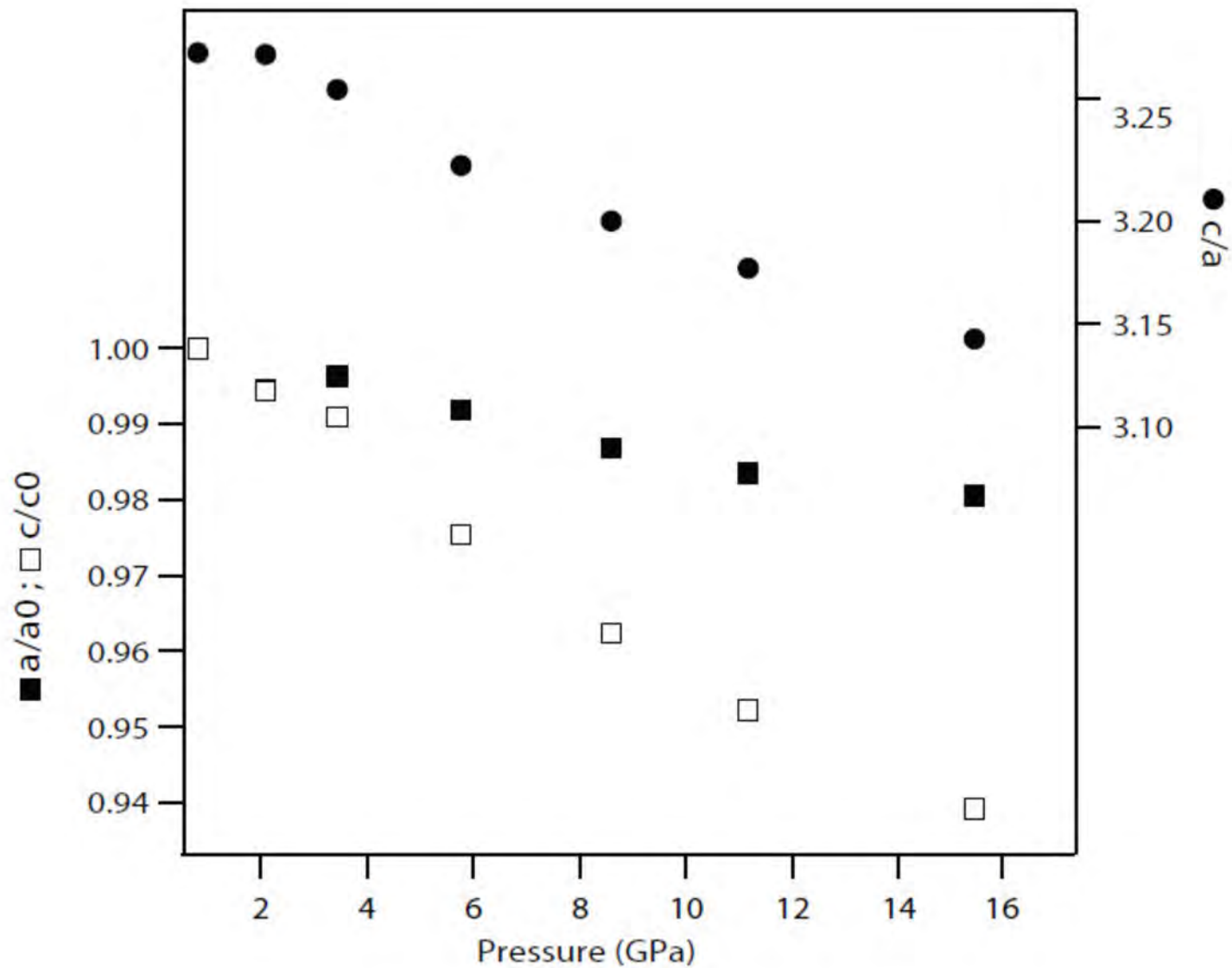


Figure 6

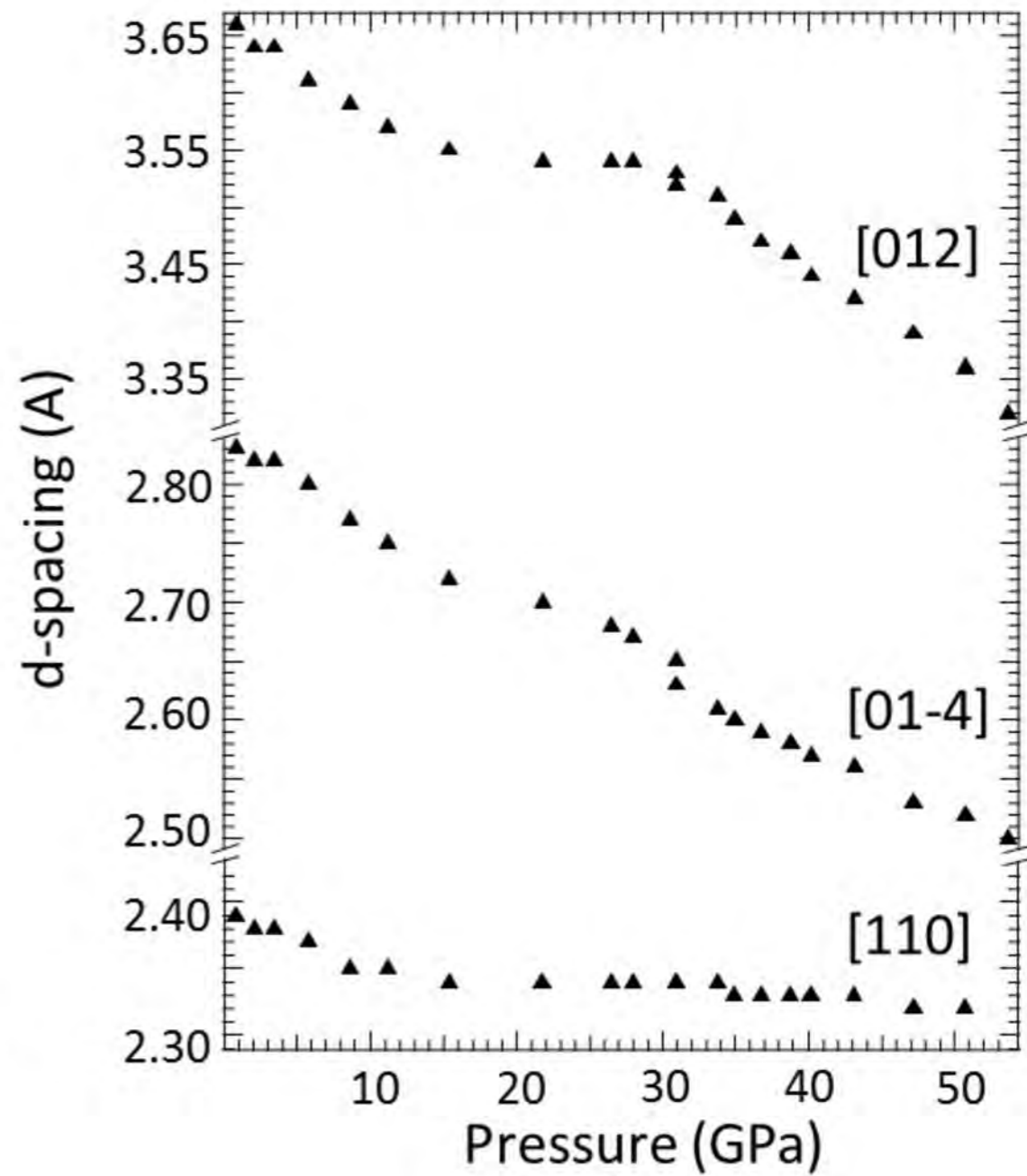
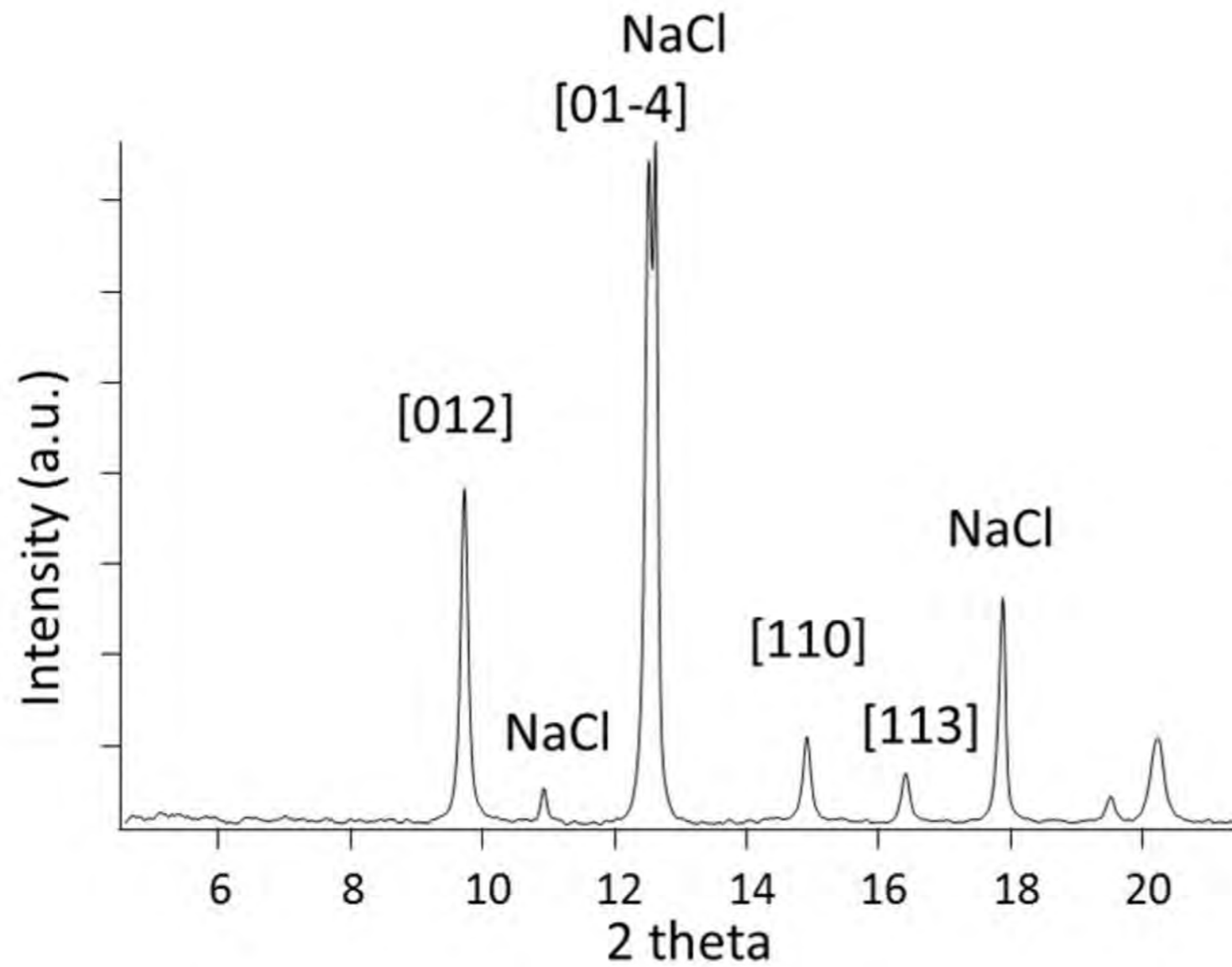


Figure 7

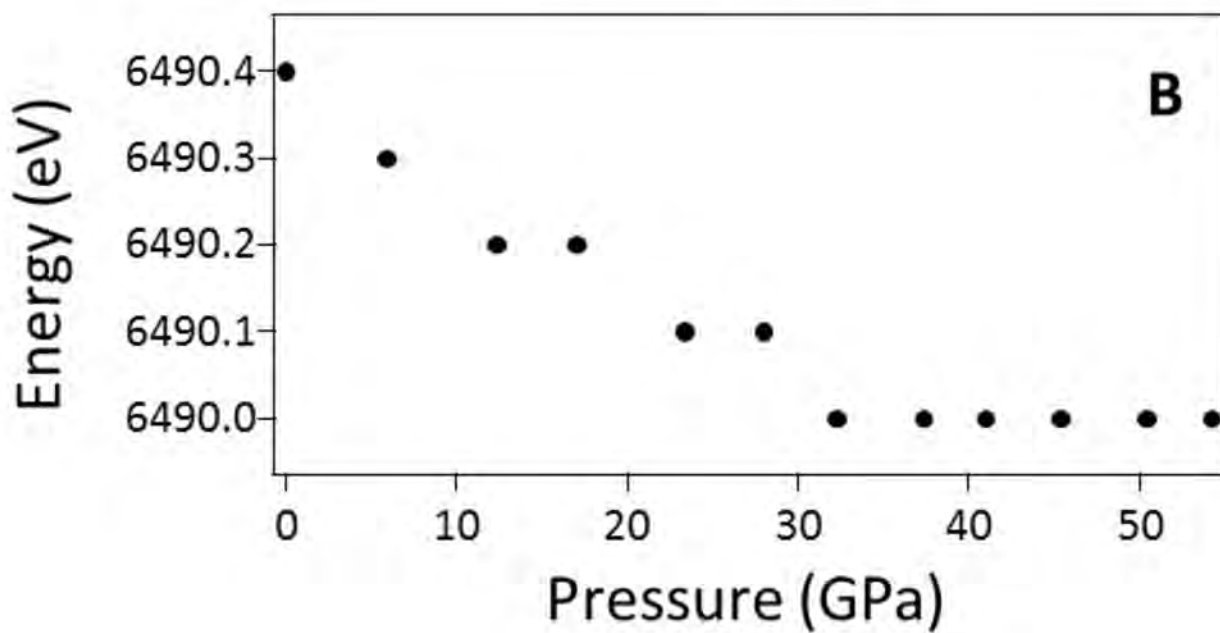
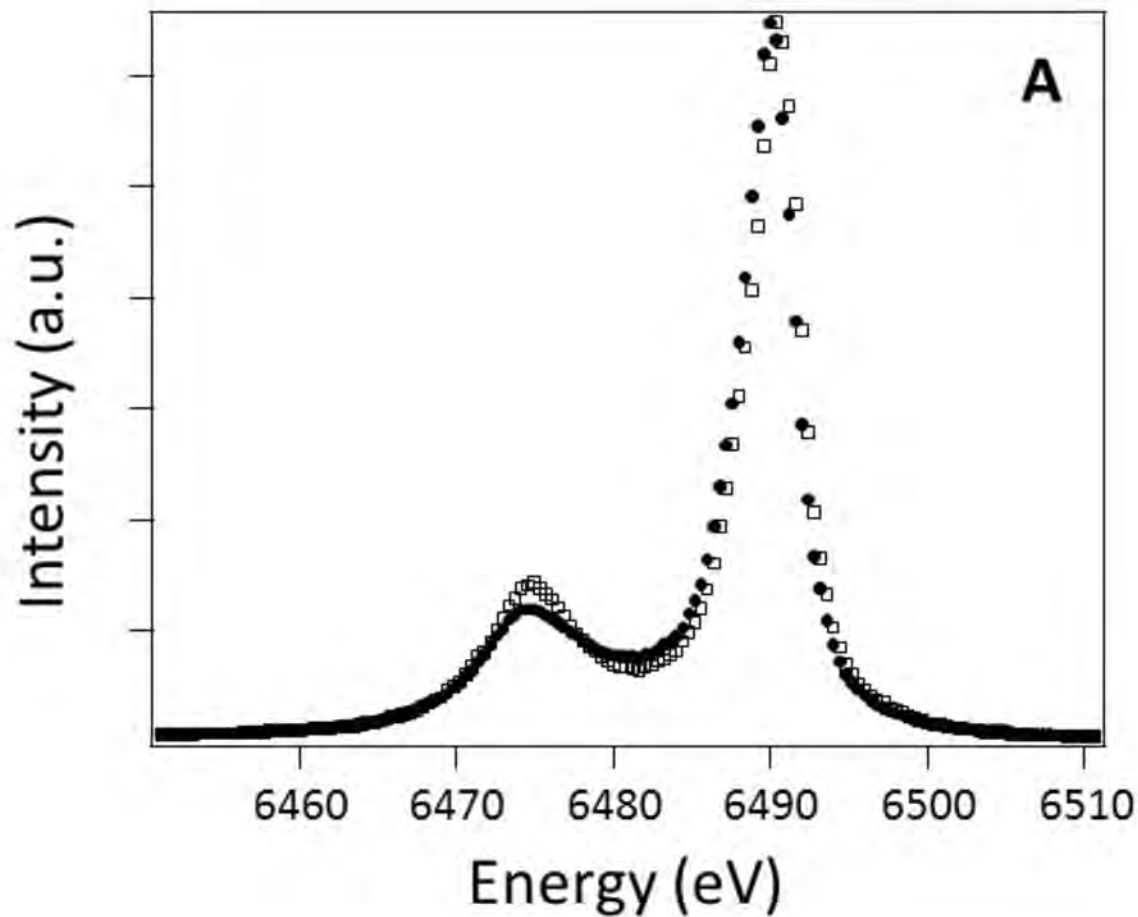


Figure 8